Materials Today Communications 42 (2025) 111415

Contents lists available at ScienceDirect

Materials Today Communications

journal homepage: www.elsevier.com/locate/mtcomm

Effect of N_2 ratio on the conductivity and corrosion resistance of TiN/TaN coating on TC4 bipolar plates for PEMFC

Wei Li [a,*], Yong Wang [a], Xiulan Li [a], Xinjun Zhou [a], Lintao Liu [b], Xuan Li [a], Xiao Jiang [a], Can Xiong [a], Yao Chen [a], Fei You [a]

[a] Faculty of Mechanical Engineering, Sichuan University of Science & Engineering, Yibin 644000, China
[b] Northwest Institute for Nonferrous Metals Research, China

ARTICLE INFO

Keywords:
PEMFC
TC4 Bipolar Plates
Nitride coatings
Corrosion resistance
Interfacial contact resistance

ABSTRACT

To enhance the corrosion resistance and conductivity of TC4 bipolar plates in Proton Exchange Membrane Fuel Cells (PEMFCs) environments, a TiN/TaN bilayer coating was prepared using radio-frequency (RF) and direct-current (DC) magnetron sputtering at various N_2 ratios. The N_2 ratio significantly affects the microstructure and phase composition of the coating. As the N_2 ratio increases, the thickness of the TiN layer increases while that of the TaN layer decreases, resulting in an improved nitride content in the coating. At an optimal N_2 ratio of 30 %, the columnar crystal structure is reduced, leading to improved coating compactness. Consequently, the corrosion current density of the TiN/TaN-30 % sample is as low as 0.0654 μA/cm^2, with corrosion currents remaining stable at 0.152 μA/cm^2 and 0.628 μA/cm^2 during constant potential polarization at 0.6 V (SCE) and 1.1 V (SCE), respectively. Additionally, the TiN/TaN-30 % sample exhibits exceptional interfacial contact resistance (ICR) values of 6.85 mΩ·cm^2 and high hydrophobicity of 95.5°. These results meet the U.S. Department of Energy standards set for 2025. This work demonstrates that TiN/TaN composite coatings have significant potential for surface modification of PEMFC metal bipolar plates.

1. Introduction

The increasing global greenhouse gas emissions and the rapid depletion of fossil energy resources highlight the urgent need to explore sustainable green energy alternatives [1]. Hydrogen, recognized as a green and clean energy source, plays a pivotal role in meeting global carbon neutrality targets [2–4]. Proton Exchange Membrane Fuel Cells (PEMFCs) are a non-polluting alternative to fossil fuels that use hydrogen and oxygen as the reaction feedstock and exhibit a high energy conversion rate (40 %-60 %) [5–7]. As a crucial component of PEMFCs, bipolar plates perform essential functions, including separating oxidants and reductants, collecting current, and facilitating the removal of residual water. Consequently, bipolar plates are required to exhibit high corrosion resistance, excellent electrical conductivity, and significant hydrophobicity [8–10]. The commonly used PEMFC bipolar plate materials mainly include metal, graphite, and composite materials [11–13]. Among these, metal bipolar plates are increasingly favored due to their low production cost, superior machinability, and outstanding conductivity. The primary materials for metal bipolar plates are stainless steel, aluminum alloys, titanium, and titanium alloys. However, in the PEMFC environment, stainless steel releases metal ions such as Fe^{3+}, Cr^{3+}, Cr^{6+}, and Ni^{2+}, which accelerate the corrosion of the membrane electrode assembly (MEA). Aluminum alloys, while possessing better conductivity, exhibit corrosion rates an order of magnitude higher than stainless steel in the PEMFC environment, with the passivation film formed on their surface significantly reducing the PEMFC's service life [14–16]. Compared with other metals, titanium and titanium alloys have garnered significant research attention due to their high specific strength, exceptional corrosion resistance, and relatively low toxicity of Ti ions to the MEA [17,18]. Nevertheless, titanium bipolar plates are susceptible to minor corrosion in the acidic and high-temperature environment of PEMFCs (pH=2–5, 70–80 °C). Furthermore, the corrosion products and passivation films that spontaneously form on titanium surfaces increase the interfacial contact resistance (ICR), significantly reducing conductivity and PEMFC output efficiency [19].

To address the challenges of titanium bipolar plate corrosion and conductivity loss, surface modification has emerged as a mainstream solution. Common surface modification techniques for metal bipolar

* Corresponding author.
E-mail address: liweibuqi@163.com (W. Li).

https://doi.org/10.1016/j.mtcomm.2024.111415
Received 1 October 2024; Received in revised form 3 December 2024; Accepted 22 December 2024
Available online 24 December 2024

plates include plasma nitriding [20], electroless plating [21,22], high-velocity oxygen fuel (HVOF) spraying [23], physical vapor deposition (PVD) [24], chemical vapor deposition (CVD) [25,26], electrochemical insertion [27], and thermal reaction deposition [28]. Among these, PVD has gained prominence due to its advantages, such as low deposition temperature, high efficiency, sound diffraction, and the ability to produce a wide variety of coatings [29]. The preparation of transition metal nitride coatings via PVD has been extensively studied as a cost-effective and efficient approach to enhancing the corrosion resistance and electrical conductivity of titanium bipolar plates [30,31]. TiN coatings, in particular, offer several advantages, including low cost, high hardness, excellent corrosion resistance, and high conductivity (up to 4.55 $\times 10^6$ S/m). Additionally, the thermal expansion coefficient difference between TiN and titanium is minimal (only 0.63 %), which effectively alleviates stress at the coating-substrate interface, promoting strong adhesion [32–34]. Heo et al. [35] demonstrated that arc-ion plating technology can produce TiN coatings with minimal porosity, reducing the corrosion current density to below 1 μA/cm^2 in both anodic and cathodic PEMFC environments. Tantalum-based coatings, such as TaN, have also shown promise due to their low resistivity, exceptional chemical stability, and broad passivation potential range, particularly in harsh PEMFC environments. Choe et al. [36] reported that TaNx coatings effectively improved the corrosion resistance of SS316L, achieving an ICR of only 11 mΩ·cm^2 under a compaction force of 150 N/cm^2. Nevertheless, metal nitride coatings prepared using physical vapor deposition (PVD) technology will inevitably exhibit a columnar structure, as with most coatings. Corrosive liquids can penetrate the coating through gaps in the columnar structure, leading to localized corrosion. To address this, multilayer coatings have been explored to reduce the pathways for corrosive liquid infiltration, thereby enhancing corrosion resistance. For instance, Pan et al. [37] demonstrated that CrC/CrN multilayer coatings deposited on SS304 using reactive magnetron sputtering exhibited superior corrosion resistance and conductivity compared to single-layer CrN coatings in PEMFC environments. Similarly, studies by Jannat et al. [38] and Wang et al. [39] confirmed that multilayer coatings effectively mitigate pinhole corrosion defects and provide enhanced protection for metal bipolar plates. However, although the design of a multilayer structure coating based on metal/-metal nitride can reduce the probability of corrosive liquid invading the substrate, there is often a significant potential difference between the metal and the metal nitride. When corrosive liquids infiltrate the interface between metal and nitride layers, galvanic corrosion can occur, posing challenges for long-term PEMFC operation [40,41].

The growth of metal nitride coatings in PVD processes is typically governed by the reaction between sputtered metal atoms and nitrogen atoms in the chamber. Notably, variations in the nitrogen (N_2) ratio during deposition significantly influence the composition, structure, and roughness of the resulting nitride coatings, which directly impact coating defects, conductivity, and corrosion resistance [42]. Current research on the effect of the N_2 ratio has primarily focused on single-layer nitride coatings [43], with limited understanding of its influence on multilayer structures and their corrosion mechanisms in PEMFC environments. Therefore, it is significant to study the effect of the N_2 ratio on the microstructure and performance of multilayer nitrides in the PEMFC environment. Thus, this study employs RF and DC reactive magnetron sputtering technology to fabricate a double-layer TiN/TaN composite coating on the TC4 surface with different N_2 ratios (10 %, 20 %, 30 %, 40 %, 50 %). The effect of the N_2 ratio on the structural properties, electrochemical behavior, conductivity, and hydrophobicity of the TiN/TaN coating was systematically characterized and analyzed under a simulated PEMFC environment. Additionally, the mechanism of the N_2 ratio on coatings' corrosion resistance and conductivity was revealed, and valuable guidance was provided for designing and optimizing protective coatings for bipolar plates.

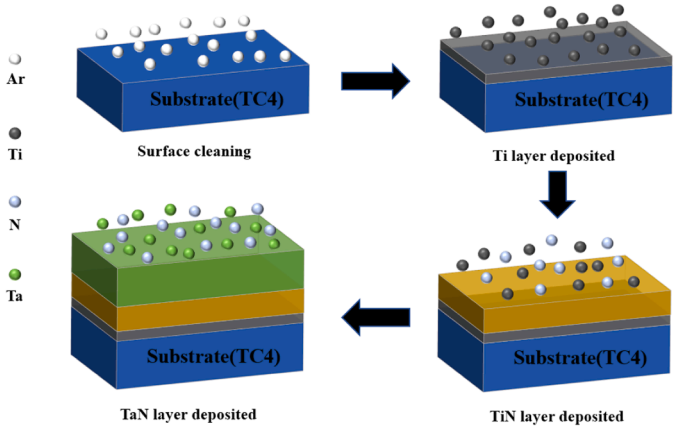

Fig. 1. Flow chart of coating preparation.

2. Experimental materials and methods

2.1. Deposition of coating

Single crystal silicon (001) and TC4 (Ti-6Al-4V) titanium alloy (15 mm × 15 mm × 1 mm) were chosen as substrates. Cross-sectional analysis of the coatings was conducted on the single-crystal silicon substrate, while microscopic characterization and performance testing were carried out on the TC4 samples. Prior to coating deposition, the samples were ultrasonically cleaned in ethanol and acetone for 15 minutes to remove surface contaminants, followed by drying under an N_2 atmosphere. The coating preparation was conducted at a temperature of 300 °C using a magnetron sputtering system that employed a high-purity titanium target as the RF target and a high-purity tantalum target as the DC target. The vacuum chamber was pumped to below 1.5 × 10^{-3} Pa before deposition, and the substrate was bombarded with argon ions at −800 V bias for 30 min to remove the contaminant from the sample surface. During deposition, the bias voltage was adjusted to −50 V. Initially, a radio frequency titanium target with a power of 200 W was used to prepare the Ti bonding layer to ensure adhesion between the coating and the substrate. Then, the titanium target power was reduced to 150 W, and N_2 was introduced to facilitate the deposition of the TiN transition layer. After the TiN layer deposition was completed, the RF titanium target was turned off without changing the N_2 ratio, the DC tantalum target was turned on, and the current was set to 0.3 A to deposit the TaN layer. The deposition pressure for all coatings was maintained at 6 × 10^{-1} Pa. The Ti bonding layer was deposited in Ar atmosphere, while the TiN transition layer and TaN layer were deposited in a mixed atmosphere of Ar and N_2.The experiment was completed by preparing five distinct TiN/TaN coatings at varying N_2 ratio percentages of 10 %/20 %/30 %/40 %/50 %. The detailed coating preparation process and process parameters are shown in Fig. 1 and Table 1.

2.2. Microstructural characterization

The surface and cross-sectional micro-morphological and structural characteristics of the coatings were analyzed using a scanning electron microscope (SEM) type VEGA3SUB (TEScan, Czech Republic), with an accelerating voltage of 15 kV. The bonding composition of TaN in the surface layer was investigated using X-ray photoelectron spectroscopy (XPS, ESCALAB 250Xi, Thermo Fisher Scientific, USA). Monochromatic Al-Kα radiation with an energy of 1486.76 eV was employed as the excitation source, and the anode power was set to 72 W (12 kV, 6 mA). The spot size was 2 mm^2, and the system pressure was maintained below 1.0 × 10^{-9} mBar. Prior to spectroscopic analysis, the coated surfaces were cleaned via Ar^+ ion beam etching for 60 minutes at an energy of 2000 eV and an incidence angle of 45°. Since carbon was confirmed to

Table 1
Deposition parameters of the coating.

Step	Bias voltage (V)	Temperature(℃)	RF power(w)	DC current(A)	Air flow (sccm)	N_2 flow (sccm)	Time (min)
1	−800	0	0	0	60	0	30
2	−50	300	200	0	25	0	15
3	−50	300	150	0	22.5/20/17.5/15/12.5	2.5/5/7.5/10/12.5	60
4	−50	300	0	0.3	22.5/20/17.5/15/12.5	2.5/5/7.5/10/12.5	90

be an external contaminant, the spectrum alignment was corrected based on the sample work function (ΦSA=4.63 eV), yielding a corrected C 1 s peak position of E_B= 289.58 eV-ΦSA = 284.95 eV [44].

2.3. Electrochemical measurements

According to the electrochemical test standard established by the U. S. Department of Energy in 2025 [45], all electrochemical measurements were performed in a simulated working environment of 70 °C, 0.5 mM H_2SO_4, and 5 ppm F^-. This work conducted the electrochemical test using Huahui's electrochemical corrosion, friction, and wear tester (MFT-EC4000). The corrosion behavior of the sample was evaluated using a standard three-electrode system. The counter electrode was a platinum sheet, the reference electrode was a saturated calomel electrode (SCE), and the working electrode was the sample (the test area was 1 cm^2). Prior to electrochemical measurements, the system was stabilized for 60 minutes at the open circuit potential (OCP). The potentiodynamic polarization test range was −0.6 V to 1.2 V, with a scan rate of 1 mV/s. Potentiostatic polarization tests were conducted at 0.6 V and 1.1 V, with 7200 s and 3600 s test times, respectively. Electrochemical impedance spectroscopy (EIS) tests were carried out at an open circuit potential within a frequency range of 100 kHz to 0.01 Hz with an amplitude of 10 mV, and the test results were fitted using Zview3.3 software. Additionally, the Mott-Schottky analysis was performed at a frequency of 1000 Hz, scanning from 1.4 V (SCE) to −0.6 V (SCE) at a rate of 50 mV/s to further characterize the surface properties.

2.4. ICR and water contact angle measurements

The ICR values of the samples in this study were measured using the Kumar method [46]. The sample was placed between two sheets of GDL carbon paper (YLS-35, TORAY, Japan) and two pure copper plates. Using a universal testing machine, the copper plate was subjected to a compression force ranging from 20 N/cm^2 to 200 N/cm^2. The resistance value was measured using a resistance measuring instrument (TH2516B, Tonghui, China), and the ICR value of the sample was finally calculated. The average value was determined after measuring each sample three times.

The sample's water contact angle (θ) at room temperature was measured using a JC2000C contact angle meter. A 2 μm diameter micropipette was used to control the volume of distilled water droplets on the surface of the sample, and the contact angle was recorded after the droplets had stabilized on the sample surface. The average value was determined after measuring each sample three times to reduce the test error.

2.5. Coating adhesion test procedures

The ASTM D3359 standard [47], approved by various agencies of the U.S. Department of Defense, was used to evaluate coating adhesion. According to this standard, adhesion performance is graded from 0 to 5. Grade 0 represents the poorest adhesion performance, while grade 5 indicates the highest adhesion performance. In this study, the coating adhesion test was conducted using the grid method specified in Section 12 of the ASTM D3359 standard. The test utilized 3 M transparent adhesive tape (Scotch 600) and sharp razor blade.

3. Results and discussion

3.1. Micromorphology analysis

Fig. 2 illustrates the SEM microscopic morphology of the coatings under varying N_2 ratios. The coatings are continuous, free of cracks, and exhibit strong adhesion to the substrate, with no apparent defects. In the cross-sectional analysis, the Ti bonding layer is too thin to be distinctly observed due to its short deposition time. Consequently, the coating primarily consists of the outer TaN layer and the inner TiN layer. The use of RF power effectively mitigates charge accumulation on the target surface, prevents target poisoning, and enhances deposition stability. As a result, the TiN layer remains dense and uniform across all N_2 ratios, with its thickness increasing from 111 nm to 268 nm as the N_2 ratio increases. Conversely, the TaN layer, deposited using DC power, exhibits a typical columnar structure and a gradual thickness reduction from 662 nm to 231 nm with increasing N_2 content. This reduction is attributed to target poisoning caused by the reaction of N atoms with the Ta target surface, which decreases deposition efficiency. At a 10 % N_2 ratio (Fig. 2(a, b)), the columnar structure of the TaN layer is not prominent, and the coating appears dense, albeit with a rough surface containing cluster particles and voids. When the N_2 ratio increases to 20 % (Fig. 2(c, d)), the surface roughness improves, with fewer clusters and voids, while the columnar structure becomes more distinct. At 30 % N_2 ratio (Fig. 3 (e, f)), the coating achieves better densification, and the gaps between the columnar crystals in the TaN layer become less noticeable, eliminating visible surface defects. However, at 40 % (Fig. 2(g, h)) and 50 % N_2 (Fig. 2(i, j)), larger voids emerge on the surface, and pronounced columnar structures are evident across the coating thickness. These features may negatively impact the corrosion resistance of the coating.

3.2. XPS analysis

To analyze the bonding composition of the TaN layers, the high-resolution spectra of Ta4f and Ta4p/N1s were fitted using an 80 % Gaussian and 20 % Lorentzian function. As shown in Fig. 3(a-e), the Ta4f peak fitting results reveal an asymmetric double-peak structure, corresponding to Ta4f 7/2 and Ta4f 5/2. Since the samples are inevitably exposed to oxygen in the air during preparation, transfer, and storage, the peaks at 26.3 eV and 28.3 eV in the high binding energy region of Ta4f 5/2 are related to Ta-O bonds [48]. At a 10 % N_2 ratio, the peak at the low binding energy of 21.9 eV corresponds to pure metallic Ta [49]. The primary peaks of Ta4f 7/2 and Ta4f 5/2 are located at 23.1 eV and 24.95 eV, respectively, due to the contribution of Ta-N bonds [50–52]. As the N_2 ratio increases from 20 % to 50 %, the main peaks of Ta4f 7/2 shift from 23.6 eV to 23.7 eV, and those of Ta4f 5/2 shift from 25.41 eV to 25.52 eV, indicating a progressive formation of nitrogen-rich tantalum compounds [43,49]. Similarly, the peak fitting results for Ta4p/N1s (Fig. 3(f-j)) confirm the presence of N-Ta bonds, with binding energies of 398 eV (Ta4p) and 402 eV (N1s) [53]. These binding energies shift with increasing N_2 ratio, likely due to changes in coordination numbers within the TaN coating and the influence of nitrogen content [54].

Fig. 4(a) depicts the variation in the peak area ratios of different bonds in the Ta4f energy level as a function of the N_2 ratio. At a 10 % N_2 and 20 % N_2 ratio, the Ta element exists primarily as Ta monomers, Ta-N bonds, and Ta-O bonds. As the N_2 ratio increases, the percentage of the

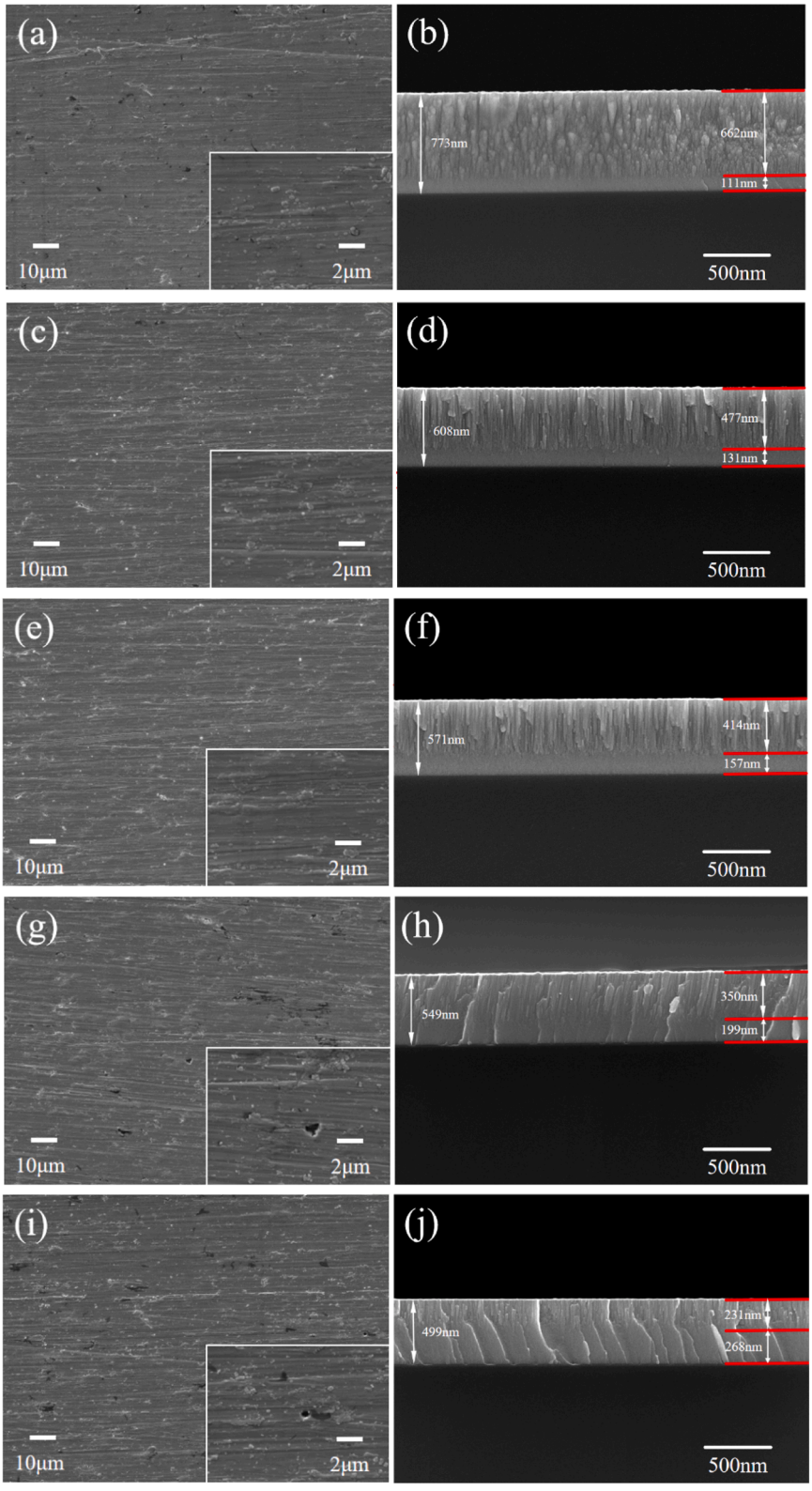

Fig. 2. SEM images of surfaces and cross-sections of different samples: (a, b) 10 %, (c, d) 20 %, (e, f) 30 %, (g, h) 40 %, and (i, j) 50 %.

Ta-N bond peak area increases, while the percentage of the Ta-O bond peak area decreases. Fig. 4(b) illustrates the relationship between the peak area ratios of Ta4p 3/2 and N-Ta bonds with respect to N_2 content. As the N_2 ratio increases, the peak area ratio of Ta4p 3/2 decreases, whereas that of N-Ta bonds increases. This trend confirms that the nitrogen content in the TaN coating rises with increasing N_2 ratio, promoting the formation of more N-Ta bonds.

3.3. Electrochemical corrosion behavior test

3.3.1. Potentiodynamic polarization test

Fig. 5 shows the samples' potentiodynamic polarization curves under

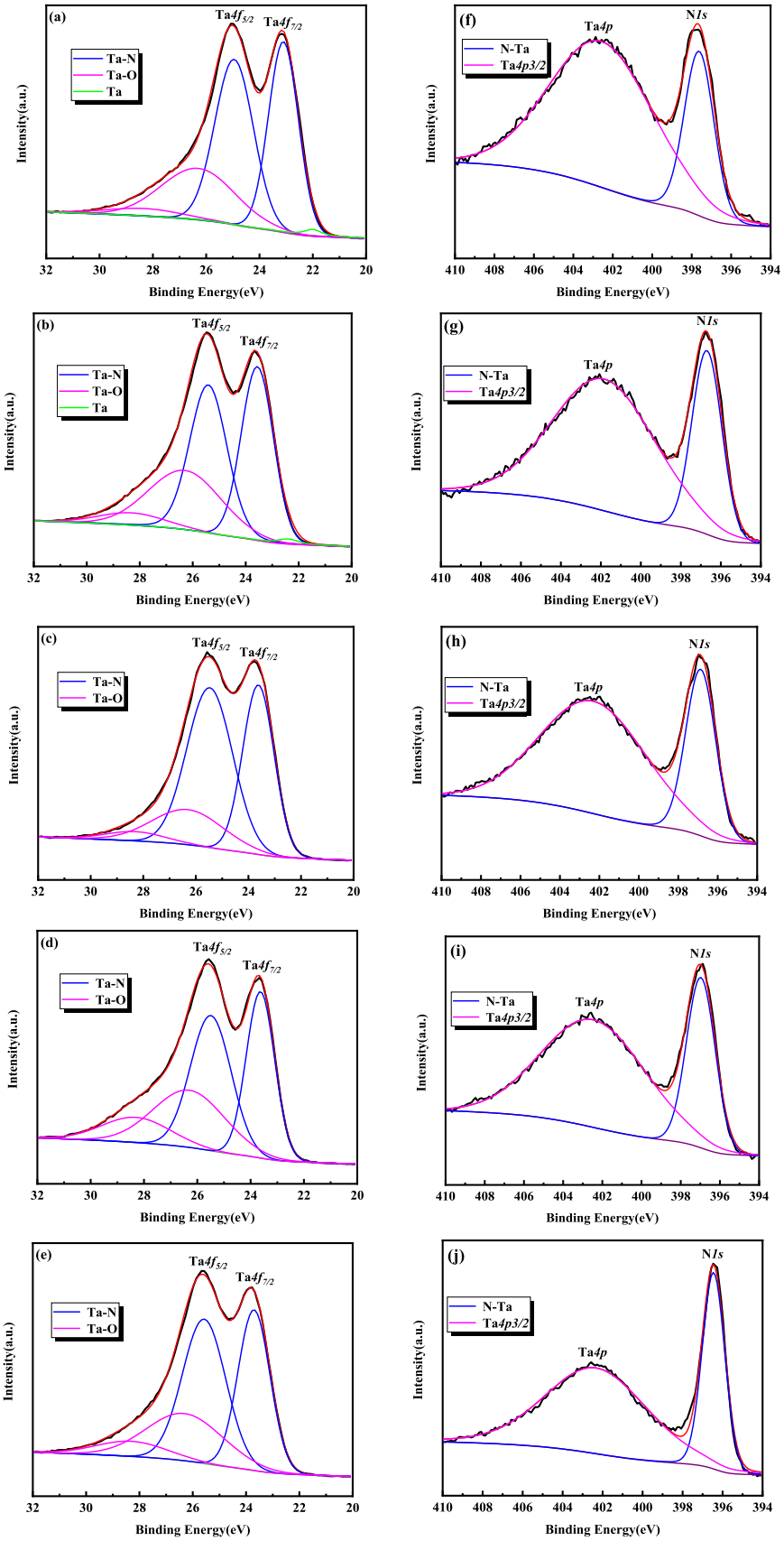

Fig. 3. XPS spectra of the (a) Ta4f and (b) Ta4p/N1s core levels for the TaN coating deposited at varying N_2 ratio: (a, f) 10 %, (b, g) 20 %, (c, h) 30 %, (d, i) 40 %, and (e, j) 50 %.

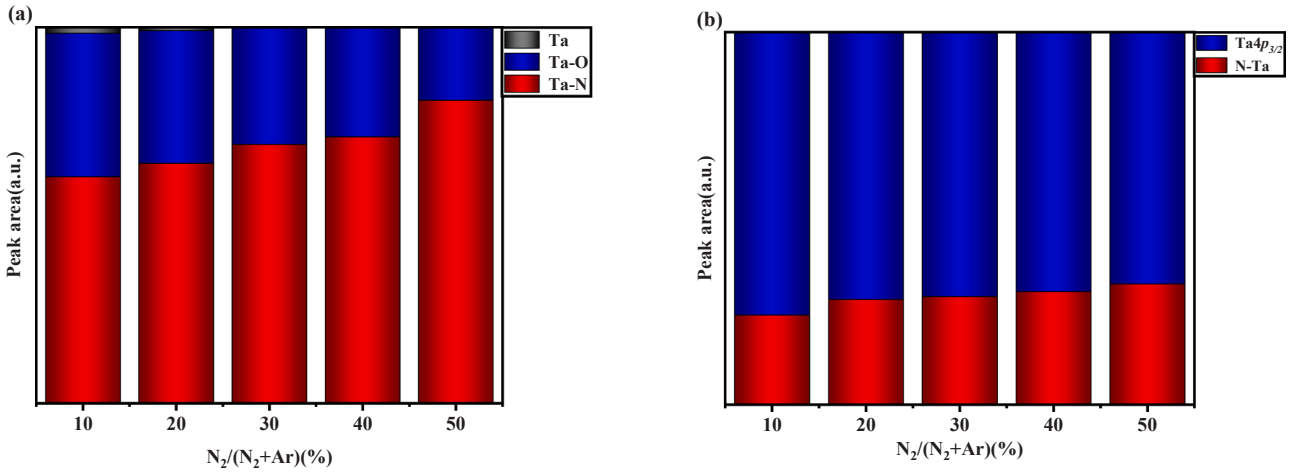

Fig. 4. Variation of the peak area of the (a) Ta4f and (b) Ta4p/N1s for the deposited TaN coating at the different N_2 ratios.

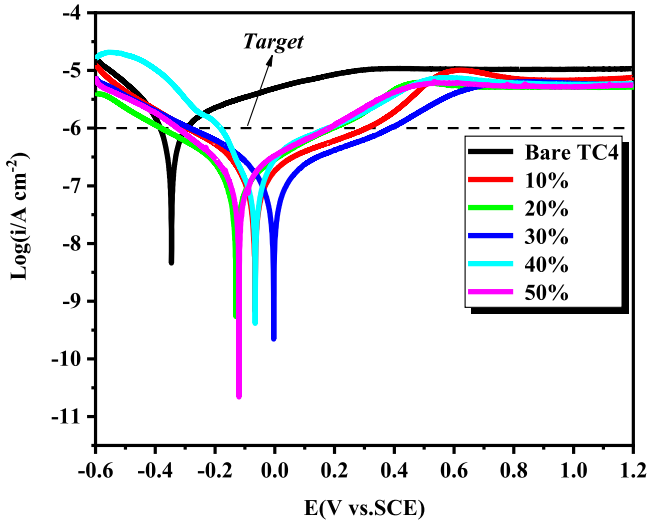

Fig. 5. Dynamic potential polarization curves of different samples.

Table 2
Electrochemical parameters of different samples.

Samples	E_{corr}/V(vs. SCE)	I_{corr}/ A·cm^{-2}	β_a/ V·dec^{-1}	β_c/ V·dec^{-1}	P_i/ %
Bare TC4	−0.345	2.99×10^{-6}	0.631	0.251	/
TiN/ TaN−10 %	−0.065	8.03×10^{-8}	0.149	0.18	97.3
TiN/ TaN−20 %	−0.129	7.63×10^{-8}	0.168	0.187	97.4
TiN/ TaN−30 %	−0.003	6.54×10^{-8}	0.151	0.184	97.8
TiN/ TaN−40 %	−0.065	8.53×10^{-8}	0.167	0.147	97.1
TiN/ TaN−50 %	−0.119	8.8×10^{-8}	0.171	0.151	97

a simulated PEMFC cathode environment (air purge electrolyte,70 °C, 0.5 mM H_2SO_4, 5 ppm F^-). The electrochemical parameters obtained by Tafel extrapolation are shown in Table 2. Compared with the TC4 substrate, the corrosion potential (E_{corr}) of all coating samples shifted to the positive direction , suggesting that they possess higher chemical inertness and thermodynamic stability [55]. Notably, the E_{corr} values of all coated samples exceed the potential of the PEMFC anode environment (-0.1 V vs. Standard Hydrogen Electrode, SHE), implying that the coating can be better cathodically protected and reduced risk to coating corrosion under anodic conditions [56]. Significantly lower corrosion current density (I_{corr}) for all coated samples compared to TC4 substrate, and all samples met the 2025 DOE standard (≤1 μA/cm^2). This indicates that the TiN/TaN coating can be an effective protective layer for the TC4 substrate. Interestingly, the I_{corr} values exhibit a trend of initially decreasing and then increasing with the N_2 ratio. Among the coatings, the TiN/TaN-30 % sample demonstrates the lowest I_{corr}, measured at 0.0654 μA/cm^2, which is two orders of magnitude lower than that of the TC4 substrate (2.66 μA/cm^2). This result is lower than the corrosion current density of the NbN coating (I_{corr}=0.225 μA/cm^2) studied by Chen et al. [43], and even nearly an order of magnitude lower than the CrC/CrN coating (I_{corr}=0.538 μA/cm^2) studied by Pan et al. [37]. The superior performance of the TiN/TaN-30 % sample can be attributed to its optimized microstructure, which minimizes the diffusion of corrosive species into the coating, thereby enhancing corrosion resistance. The protective efficiency (P_i) of the coatings, calculated using the measured I_{corr} values [57], further supports this conclusion. Here, P_i is defined as:

$$P_i = 100\% \times \left(1 - \frac{I_{corr}}{I_{corrs}}\right) \quad (1)$$

Where I_{corr} and I_{corrs} denote the corrosion current density of the coating samples and TC4 substrate, respectively. It can be found that the P_i of all coating samples exceeds 95 %, suggesting that the TiN/TaN coating has the potential to improve the corrosion resistance of the TC4 substrate substantially.

3.3.2. *Potentiostatic polarization test*

It is well established that the higher potential on the cathode side of PEMFC is likely to aggravate the corrosion of the cathode plate by corrosive media (H^+, SO_4^{2-}, F^-). Therefore, investigating the corrosion resistance of coating samples under the PEMFC cathode environment is crucial [58]. To study the long-term stability of the coating, Fig. 6(a) is the potentiostatic polarization curve of different samples under 0.6 V (SCE) simulated PEMFC cathode environment (air purge electrolyte, 70 °C, 0.5 mM H_2SO_4, 5 ppm F^-) for 2 h. It can be seen that the corrosion current density curves experienced a rapid decrease at the initial stage and then stabilized at a constant value. Fig. 6(b) shows the corrosion current density values ($I_{0.6\ V}$) of different samples. It is found that the coated TC4 exhibits a significantly lower $I_{0.6\ V}$ value, which is nearly an order of magnitude lower than that of the TC4 substrate (2.15 μA/cm^2). This suggests that the electrochemical reaction on the surface of the coated TC4 is strongly inhibited, especially in TiN/TaN-30 % samples (0.152 μA/cm^2), indicating the best protective performance.

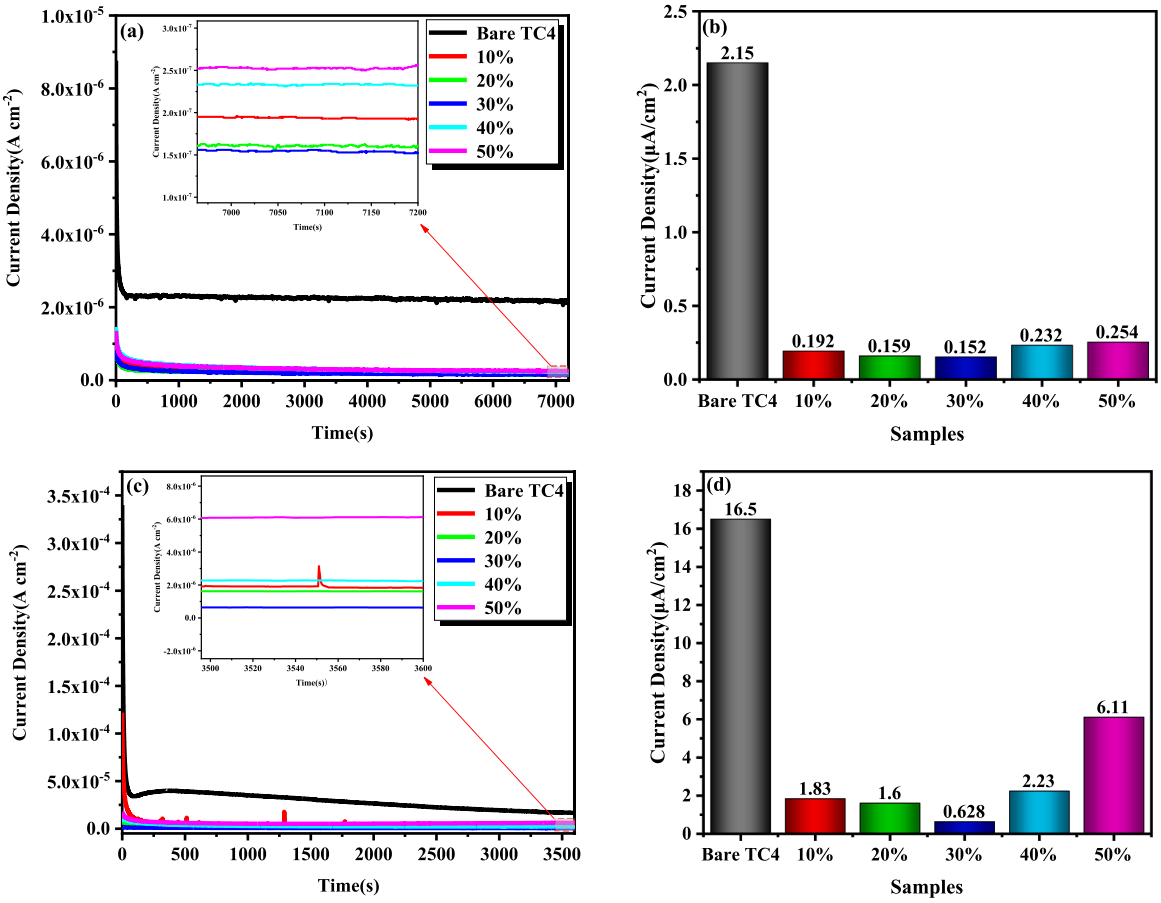

Fig. 6. (a) potentiostatic polarization curves of various samples at 0.6 V (SCE). (b) the corrosion current density measured after polarization at 0.6 V (SCE) for 2 h. (c) potentiostatic polarization curves at 1.1 V (SCE). (d) and the corrosion current density measured after polarization at 1.1 V (SCE) for 1 h.

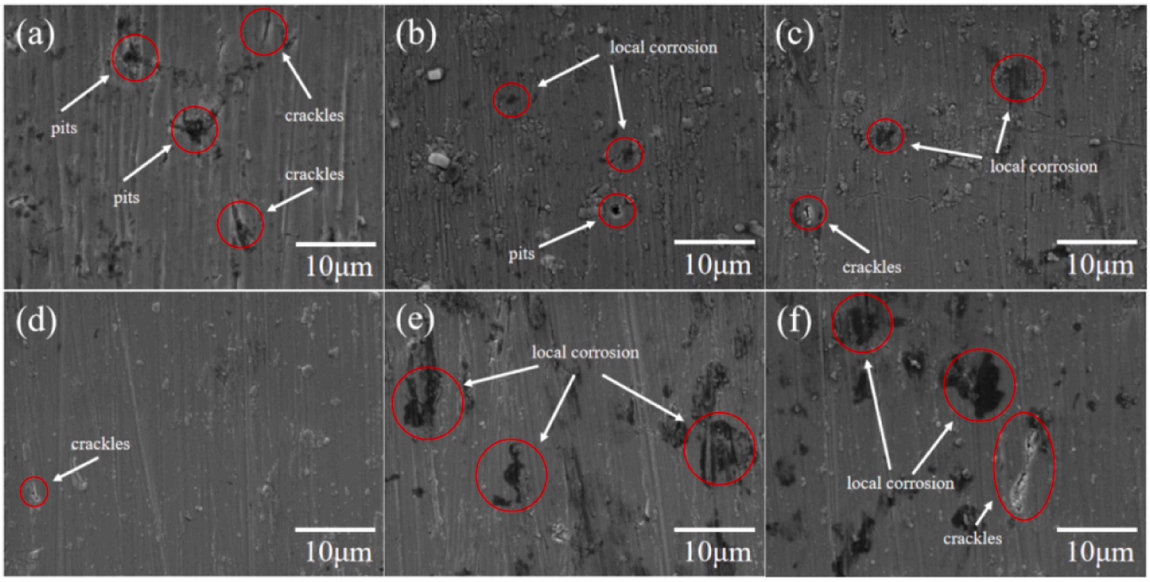

Fig. 7. Surface SEM of different samples after polarization at 1.1 V (SCE) for 1 h: (a) Bare TC4, (b) 10 %, (c) 20 %, (d) 30 %, (e) 40 %, and (f) 50 %.

During the start-up and shutdown processes of PEMFC, high potentials (0.9–1.1 V, SCE) are generated, significantly shortening the service life of the bipolar plate [59–60]. Therefore, this study assessed the long-term durability of the coating samples at a high potential of 1.1 V (SCE). Considering that the high potential generated by the vehicle under actual working conditions is instantaneous and the time is short, the high potential polarization test for 1 h can fully meet the actual operation requirements of the vehicle. The corrosion current density curve of the sample polarized at 1.1 V (SCE) potentiostatic polarization for 1 h is depicted in Fig. 6(c). Unlike the 0.6 V (SCE) test, the corrosion

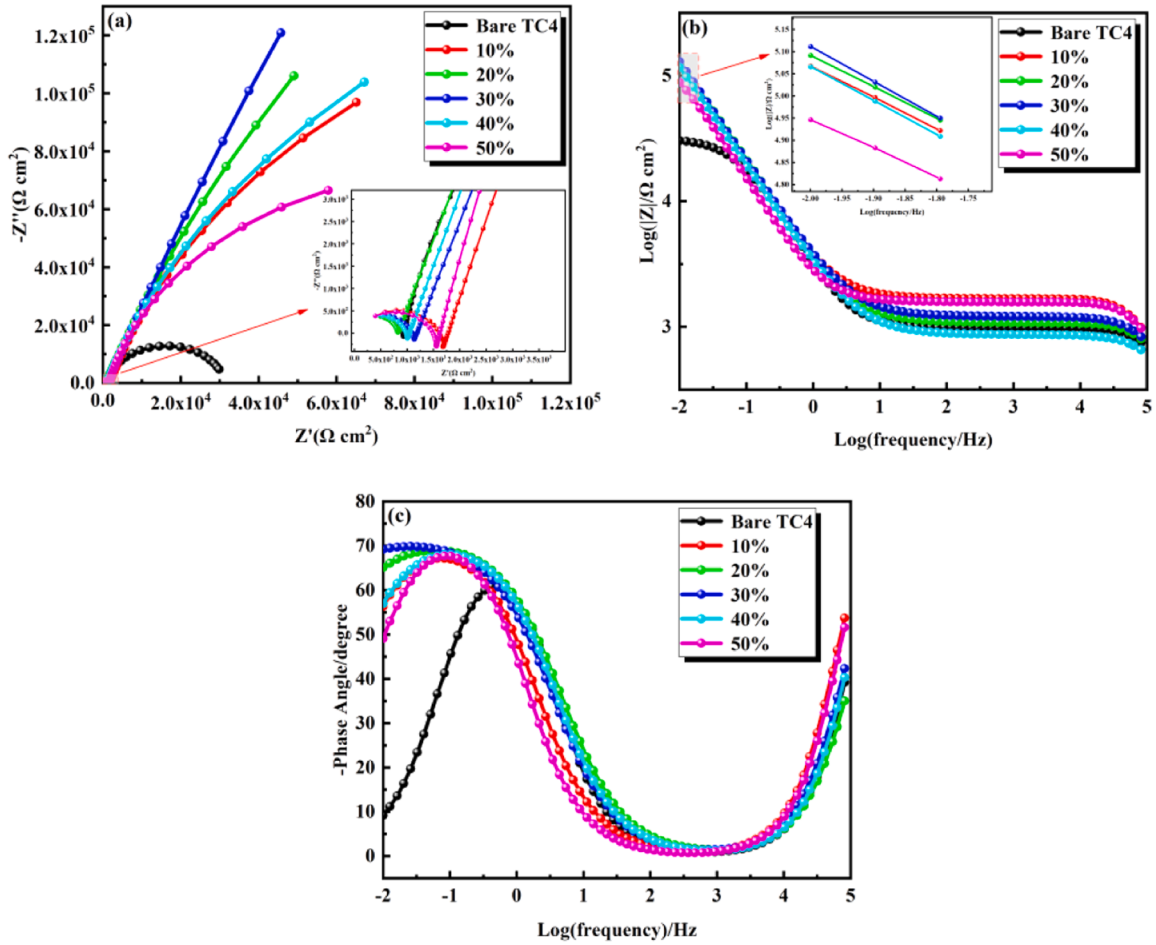

Fig. 8. EIS plots for different samples: (a) Nyquist plots. (b) Bode plots for f to Z. (c) Bode plots for f to phase angle.

current density of the bare TC4 sample decreases rapidly at 0–100 s and then rises at 100–300 s, indicating that the passivation film formed initially is unstable and cannot prevent the entry of corrosive ions under high potential. However, the passivation film form on the bare TC4 sample is thicker with the further increase of test time, so its corrosion current density gradually decreases to 16.5 μA/cm^2. In contrast, the corrosion current densities of all coated samples rapidly stabilize at significantly lower values. However, the corrosion current density curve of the TiN/TaN-10 % sample exhibited unstable fluctuations, which were the consequence of corrosion induced by a certain degree of galvanic corrosion of Ta and TaN. The corrosion current densities ($I_{1.1\ V}$) of different samples at a potential of 1.1 V (SCE) are shown in Fig. 6(d). The results imply that the $I_{1.1\ V}$ of all coating samples is lower than that of the TC4 substrate and shows a trend of initial decrease and subsequent increase as the N_2 ratio increases. The lowest $I_{1.1\ V}$ value is only 0.628 μA/cm^2 for TiN/TaN-30 %, which indicate that the high chemical stability of TiN/TaN coating even at high potentials.

The SEM morphology of the samples after the 1.1 V (SCE) potentiostatic polarization test is depicted in Fig. 7. As a result of the high potential, all samples were corroded by the corrosive ions to varying degrees, following a period of polarization. Corrosion weakened the grooves and stripes that were created by mechanical polishing. The TC4 substrate was the most severely corroded, resulting in a significant number of cracks and pits appearing on the surface following the corrosion (Fig. 7(a)). Pitting pits and local dark areas of corrosion were observed on the sample surface to varying degrees for the coating samples at lower (Fig. 7(b, c)) or higher (Fig. 7(e, f)) N_2 ratio. This may be attributed to the escalation of defects, such as holes, on the coating surface at either a higher or lower N_2 ratio. However, when the N_2 ratio was 30 %, the sample surface remained dense and uniform, with no obvious local corrosion dark areas or pitting pits (Fig. 7(d)).

3.3.3. EIS test

To qualitatively analyze the impedance characteristics of the samples, electrochemical impedance spectroscopy (EIS) tests were conducted. Fig. 8 presents the representative Nyquist and Bode plots for the various samples. The corrosive properties of all samples are similar, as evidenced by the two capacitance semicircles in the Nyquist diagram of Fig. 8(a). The semicircle diameters of all coated samples in the low-frequency region are significantly increased in comparison to the TC4 substrate, indicating that the TiN/TaN coating enhanced the corrosion resistance of the substrate. Furthermore, the diameter of the capacitive loops in the low-frequency region decreases for all samples except the TiN/TaN-30 % sample, suggesting inferior corrosion resistance of the coatings at both higher and lower N_2 ratios [61]. The high-frequency region of the Bode plot represents the contact properties between the solution and the coating, the mid-frequency region represents corrosion in the coating, and the low-frequency region represents the contact properties between the coating and the substrate [42]. The Bode impedance diagram in Fig. 8(b) and the Bode phase angle diagram in Fig. 8(c) show that the phase angles of all coated samples exhibit a plateau over a wider frequency range. Additionally, their maximum phase angles approach 90 °, in contrast to the TC4 substrate. This behavior indicates that all coated samples possess superior chemical stability in the PEMFC environment [62]. Additionally, the phase angle in the low-frequency region exhibits an initial increase followed by a subsequent decrease with rising N_2 ratios, suggesting that the susceptibility to local microporous corrosion on the coating surface decreases

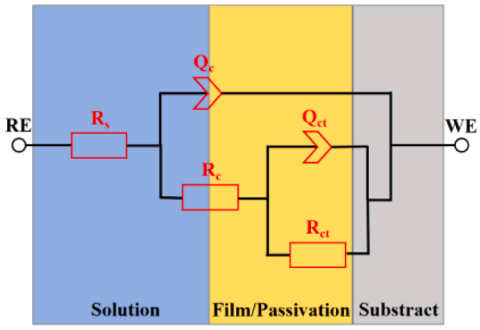

Fig. 9. Electronic equivalent circuits (EEC) used to fit the EIS spectra.

initially but increases again as the N_2 ratio continues to rise. Generally, the |Z| value in the low-frequency region indicates the corrosion resistance of the sample [5]. The TiN/TaN-30 % sample exhibits the highest corrosion resistance, as indicated by the ranking of |Z| values at 10 mHz in the low-frequency region: TiN/TaN-30 % > TiN/TaN-20 % > TiN/TaN-10 % > TiN/TaN-40 % > TiN/TaN-50 % > TC4.

To enable a qualitative analysis of the impedance characteristics of the coating samples, Zview3.3 software was used to fit the EIS measurement data. The Bode phase angle plots (Fig. 8(c)) display two distinct phase angle peaks, indicating two independent time constants for all samples. Considering that a passivation film with electrochemical properties similar to those of the coating typically forms on the TC4 surface, the impedance characteristics of both the TC4 substrate and the coating samples were fitted using an equivalent circuit model incorporating dual time constants (Fig. 9). R_s represents the solution resistance between the coating sample and the SCE, R_c represents the resistance of the corrosion product, R_{ct} denotes the charge transfer resistance, Q_c represents the capacitance of the corrosion product, and Q_{ct} is the double-layer capacitance between the coating and the substrate [63–64]. The relevant electrochemical parameters obtained through Zview3.3 software fitting are tabulated in Table 3. The R_s values of all the specimens are not significantly different, indicating that the electrochemical testing environment is relatively stable. The value of R_{ct} is significantly greater than that of R_c, so it can be assumed that the R_{ct} value is the resistance of the coating. The R_{ct} value represents the diffusion resistance of corrosive ions; a higher R_{ct} value indicates better coating protection and reduced risk to corrosion. As shown in Table 3, the R_{ct} values of all coating samples exceed those of the TC4 substrate, with the R_{ct} value of the TiN/TaN-30 % sample reaching 3.17×10^6 Ω·cm^2, indicating that the coating can forms a robust physical barrier, effectively preventing the ingress and diffusion of corrosive ions [65].

3.3.4. *Mott-Schottky test*

The passivation film formed on metals in acidic media often exhibits semiconductor properties, and the Mott-Schottky analysis is a critical method for investigating the electronic characteristics of metal passivation films [66]. Metal passivation films are generally classified as n-type or p-type semiconductors based on their electronic properties. When the applied voltage is adjusted so that the carrier concentration in the space charge region of the oxide films is in a depleted state, the space charge capacitance (C) has the following two Mott-Schottky relationships with the applied voltage (E) [67]:

For n-type semiconductors:

$$\frac{1}{C^2} = \left(\frac{2}{e\varepsilon_0\varepsilon N_D A^2}\right)\left(E - E_{fb} - \frac{KT}{e}\right) \quad (2)$$

For p-type semiconductors:

$$\frac{1}{C^2} = \left(\frac{2}{e\varepsilon_0\varepsilon N_A A^2}\right)\left(E - E_{fb} - \frac{KT}{e}\right) \quad (3)$$

Where ε is assumed to be the relative permittivity (60 for TiO_2 and 25 for Ta_2O_5 [68]), C denotes the space-charge capacitance, and ε_0 is the vacuum permittivity. E_{fb} is the flat band potential, A is the exposed area of the specimen (1 cm^2 in this study), E is the applied potential, and N_D and N_A are the relative densities of the donor and acceptor, respectively. e is the electron charge, k represents the Boltzmann's constant, and T is the temperature (K).

Fig. 10 presents the Mott-Schottky plots of surface passivation films for various samples tested at 70 °C in an environment containing 5×10^{-4} mol/L H_2SO_4 and 5 ppm F^-. All samples demonstrate a strong linear correlation within the voltage range of 0.8–1.4 V, with a positive slope (K), as depicted in Fig. 11. This result confirms that the passivation films on all sample surfaces exhibit the electronic properties characteristic of n-type semiconductors. The slope K is directly related to the carrier concentration, with electrons serving as the primary carriers. The donor density (N_D) is commonly used to assess the performance of passivation films. The N_D value can be calculated using Equation [69]: $N_D = 2/e\varepsilon_0\varepsilon K$. Table 4 summarizes the N_D values for different samples. According to the Point Defect Model (PDM), interface reactions are primarily governed by the carrier concentration, such as cations or oxygen vacancies. The N_D values of all coating samples are lower than that of the TC4 substrate, indicating that the TiN/TaN coating effectively reduces vacancy-type defects and prevents the penetration of corrosive ions into the TC4 substrate. The N_D values of the coating samples

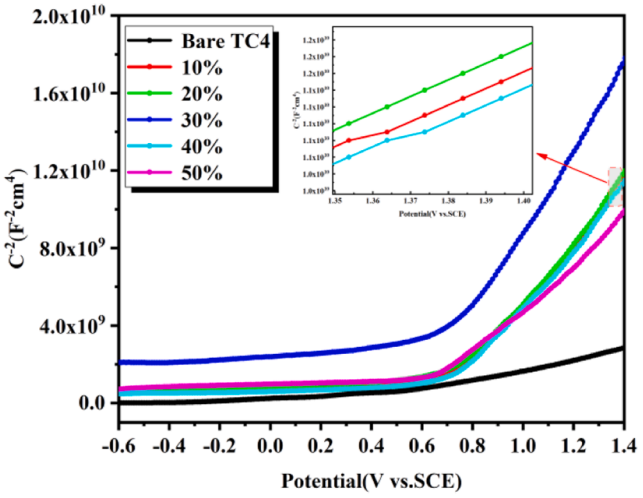

Fig. 10. Mott-Schottky plots of different samples in a simulated PEMFC cathodic environment.

Table 3
Electrochemical parameters obtained from equivalent circuits simulation.

Samples	R_s (Ω·cm^2)	R_c (Ω·cm^2)	Q_c (F·cm^2)	N_c	R_{ct} (Ω·cm^2)	Q_{ct} (F·cm^2)	N_{ct}
Bare TC4	5.61	9.86×10^2	4.28×10^{-9}	0.925	3.06×10^4	6.99×10^{-5}	0.891
TiN/TaN−10 %	5.20	1.68×10^3	2×10^{-9}	1	3.69×10^5	7.41×10^{-5}	0.928
TiN/TaN−20 %	5.09	8.68×10^2	1.59×10^{-9}	0.951	9.21×10^5	7.59×10^{-5}	0.904
TiN/TaN−30 %	5.33	1.21×10^3	1.57×10^{-9}	0.982	3.17×10^6	6.72×10^{-5}	0.968
TiN/TaN−40 %	5.06	1.08×10^3	2.02×10^{-9}	0.955	4.28×10^5	6.84×10^{-5}	0.916
TiN/TaN−50 %	5.17	1.57×10^3	2.87×10^{-9}	1	1.82×10^5	9.82×10^{-5}	0.966

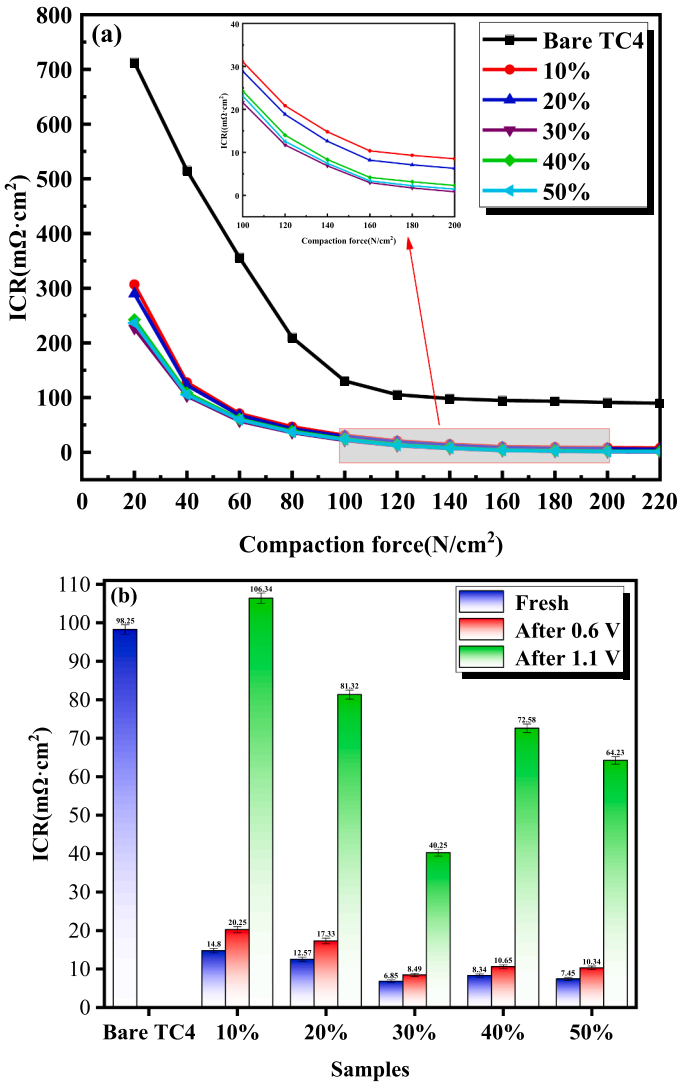

Fig. 11. (a) ICR of uncoated and coated TC4 samples under different compact forces. (b) ICR of the different samples before and after constant potential polarization.

Table 4
Characteristic parameters of n-type semiconductors of surface passivation films of different samples in a simulated PEMFC cathode environment.

Sample	Potential range(V)	$N_D(cm^{-3})$
Bare TC4	0.8 V−1.4 V	8.333×10^{20}
TiN/TaN−10 %	0.8 V−1.4 V	4.777×10^{20}
TiN/TaN−20 %	0.8 V−1.4 V	3.587×10^{20}
TiN/TaN−30 %	0.8 V−1.4 V	2.657×10^{20}
TiN/TaN−40 %	0.8 V−1.4 V	3.676×10^{20}
TiN/TaN−50 %	0.8 V−1.4 V	3.619×10^{20}

initially decrease and then increase with rising N_2 ratios. The lowest N_D value, measured at 2.657×10^{20} cm^{-3} for the 30 % N_2 ratio sample, indicates minimal defect density, consistent with the electrochemical corrosion test results.

3.4. ICR and water contact angle measurements

Excessive contact resistance in the bipolar plate during PEMFC operation generates substantial heat within the fuel cell. This leads to considerable power loss, adversely affecting the overall output performance of the PEMFC [70–71]. Fig. 11(a) illustrates the ICR curves of fresh samples subjected to varying compaction forces. At the initial stage of pressurization, the ICR values of all samples decreased sharply with increasing compaction force. This phenomenon is attributed to the increased compaction force, which improves the effective contact area between the sample and the carbon paper, thereby enhancing electron transfer efficiency. The ICR values of the TC4 substrate were consistently higher than those of the coated samples across all test pressures, indicating a significant enhancement in the conductivity of the coated TC4. Fig. 11(b) illustrates a comparison of the ICR values of all fresh samples under a compaction force of 140 N/cm^2. The ICR value of the TC4 substrate in its initial state is the highest, measuring 98.25 mΩ·cm^2, due to the presence of thick passivation films on its surface. In contrast, the coating samples exhibited significantly lower ICR values, with the 30 % N_2 ratio sample achieving the lowest value of 6.85 mΩ·cm^2. This value is notably lower than the 9 mΩ·cm^2 reported for single-layer TaN_x coatings in the study by Mendizabal et al. [72].

Notably, the ICR value of the TC4 substrate increases significantly after polarization at 0.6 V (SCE) and 1.1 V (SCE) (Fig. 11(b)). This phenomenon may be attributed to surface roughening caused by corrosion, which reduces the contact area with the carbon paper and promotes the formation of a more insulating passivation film in the PEMFC environment. The ICR values of all coating samples exhibited minimal changes after polarization at 0.6 V (SCE), indicating that the coatings maintain high electrical conductivity at this voltage. However, the ICR values of the coating samples increase significantly after polarization at a high potential of 1.1 V (SCE). This is attributed to the more severe corrosion of the coating under high potential, leading to a roughened surface and an increased number of pores and cracks (Fig. 8).

The cathodic reaction during PEMFC operation generates a significant amount of water as a by-product. However, inadequate water discharge can hinder fuel supply and reduce catalytic reaction efficiency. The removal of water from the channels is influenced not only by runner design but also by the hydrophobicity of the bipolar plate [73]. Therefore, in addition to good corrosion resistance and electrical conductivity, bipolar plates should also exhibit high hydrophobicity. The hydrophobicity of bipolar plates is typically influenced by their surface energy and roughness. Fig. 12 presents the water contact angles of both the bare and coated TC4 samples. The water contact angle of the bare TC4 sample was only 66.6°, whereas, after coating, the contact angle increased to over 90°, indicating the high hydrophobicity of the coating. It is noteworthy that the contact angle of the coating initially increases and then decreases as the N_2 ratio rises, reaching a maximum of 95.5° for the 30 % N_2 ratio sample (Fig. 13(d)). This value is significantly lower than the contact angle of the Cr_xN_y coating (89.4°) reported by Li et al. [74], demonstrating its superior hydrophobic properties. This is primarily due to the increase in TaN content with the rising N_2 ratio, leading to a gradual reduction in the surface energy of the coating. However, when the N_2 ratio exceeds 30 %, increased surface defects lead to higher roughness, which reduces the water contact angle of the coating. The high hydrophobicity of the bipolar plate aids in water management within the battery and reduces the contact between the bipolar plate and the PEMFC electrolyte solution, thereby enhancing the output power of the PEMFC.

3.5. Anti-corrosion and conductive mechanism

The corrosion resistance of the coating is mainly related to the coating microstructure (such as defects and cracks) and coating chemical stability. In this study, TiN and TaN layers, both exhibiting excellent corrosion resistance, were chosen to form a bilayer structure, thereby reducing the likelihood of pinhole penetration. Additionally, the low potential difference between TiN and TaN minimizes the risk of galvanic corrosion, thereby enhancing the overall corrosion resistance of the coating. At a 10 % N_2 ratio, the coating exhibits a bilayer structure, with a thicker TaN layer and a small, connected columnar crystal structure,

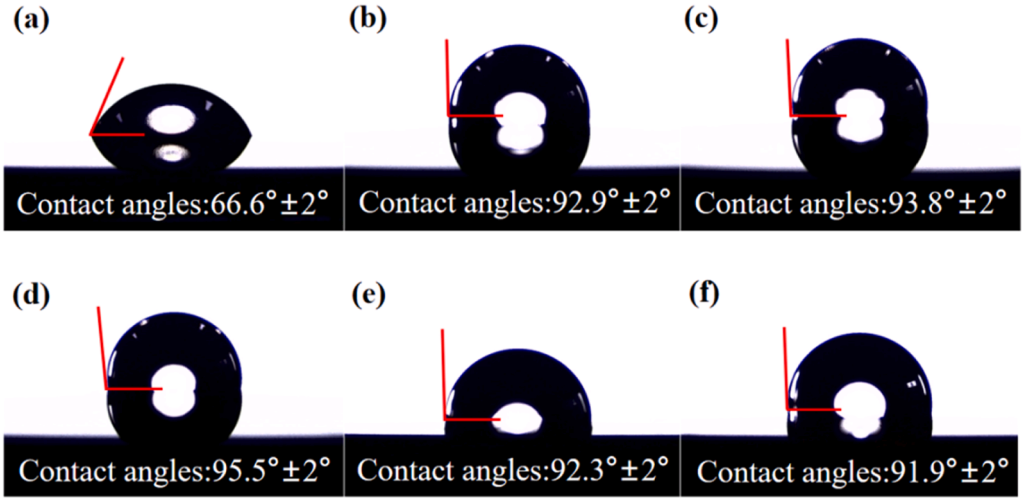

Fig. 12. Water contact angle of different samples: (a) Bare TC4, (b) 10 %, (c) 20 %, (d) 30 %, (e) 40 %, and (f) 50 %.

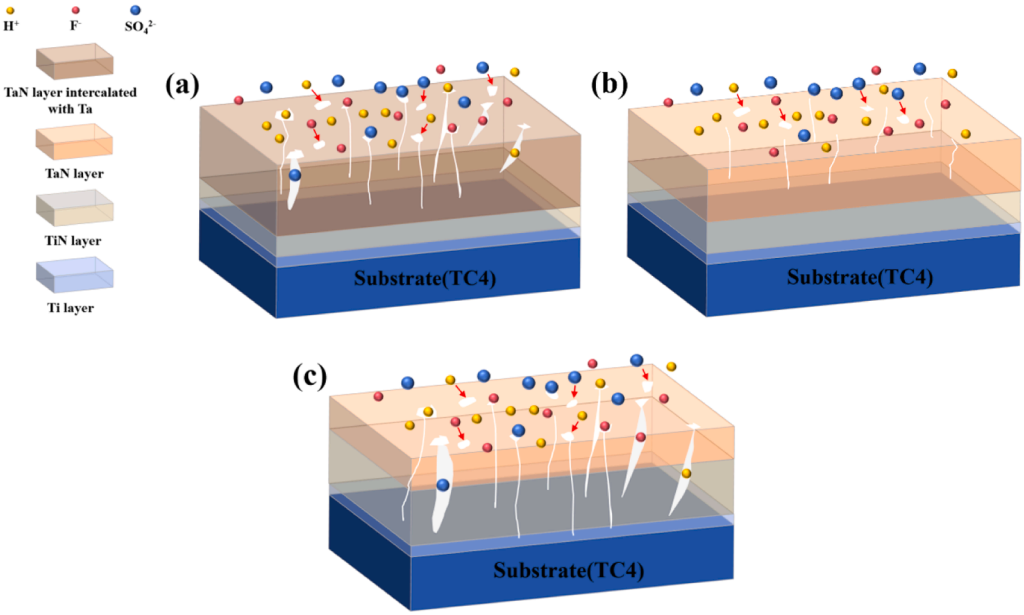

Fig. 13. Corrosion mechanisms of coated samples at 10 % (a), 30 % (b), and 50 % (c) N_2 ratio.

resulting in a relatively compact coating. However, XPS analysis reveals the presence of a small amount of Ta monomers in the TaN layer due to the low N_2 ratio. While the corrosion resistance of metal Ta is weaker than that of the TaN phase, so even though its structure is relatively dense, its corrosion current density is still high (0.0803 μA/cm^2). The cumulative invasion of corrosive liquid is expected to induce severe galvanic corrosion, accelerating the dissolution of the TaN layer and ultimately leading to the corrosion of the TC4 substrate (Fig. 13(a)). As the N_2 ratio gradually increases to 30 %, the TaN content rises, and the TaN layer develops a more defined columnar structure. Meanwhile, the dense TiN layer thickens, and diffusion channels for corrosive ions primarily form in the TaN layer. Even if a small amount of corrosive liquid enters the TaN layer, it will be blocked by the TiN layer, so the corrosion current density of the coating gradually decreases to 0.0654 μA/cm^2, achieving better protection for the TC4 substrate (Fig. 13(b)). Potentiodynamic polarization and Mott-Schottky tests show that the coating exhibits the lowest defect density (2.657 $\times 10^{20}$ cm^{-3}) and the highest protection efficiency (97.8 %) when prepared with a 30 % N_2 ratio. Notably, at a high corrosion potential of 1.1 V (SCE), owing to the unique double-layer structure and the excellent corrosion resistance of the TiN/TaN-30 % coating, the corrosion current remains stable at 0.628 μA/cm^2 under high-voltage corrosion conditions. However, at higher N_2 ratios (40 %, 50 %), columnar crystal structures that from the surface penetrate to TC4 substrate appeared in the coating. The corrosive liquid can directly pass through the coating through these gaps between the columnar crystals, resulting in the local corrosion of the TC4 substrate (Fig. 8(e, f)), seriously reducing the corrosion resistance of the coating (Fig. 13(c)).

The electrical conductivity of the bipolar plate surface is closely related to the surface morphology (particle size, cavity) and the resistivity of the surface phase. XPS analysis shows that the relative content of Ta-N bonds in the TaN layer increases with the rising N_2 ratio. In contrast, the relative content of Ta-O bonds decreases gradually (Fig. 4). An increased Ta-N bond ratio and a decreased Ta-O bond ratio enhance interfacial charge transfer efficiency, thereby improving conductivity. However, the enhancement of coating conductivity results from the combined effects of surface microstructure and the bonding composition of the coating. At both lower and higher N_2 ratios, the surface roughness

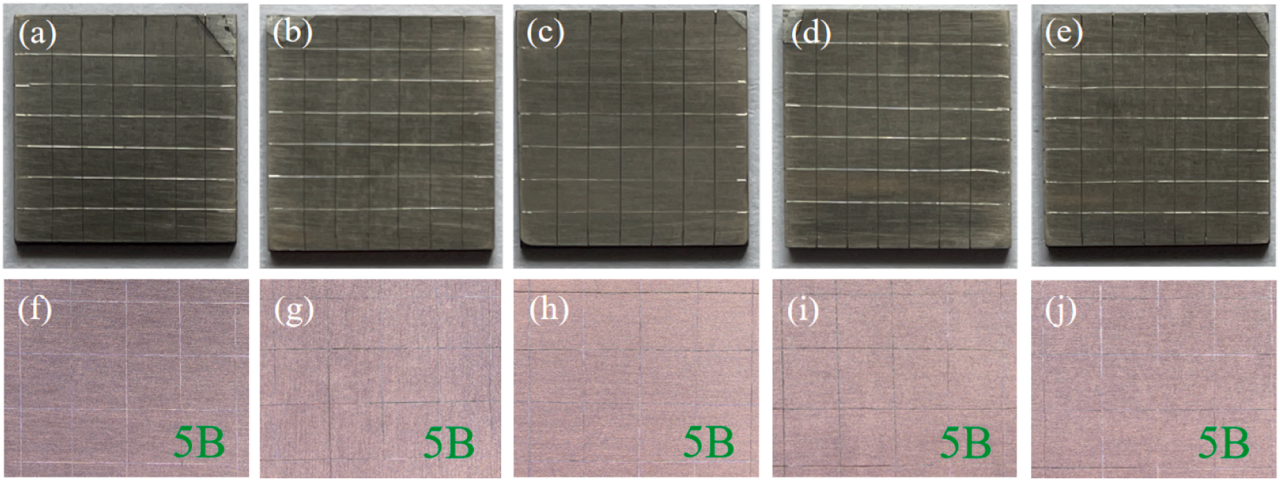

Fig. 14. The photographs of different TiN/TaN coatings after adhesion test: (a, f) 10 %, (b, g) 20 %, (c, h) 30 %, (d, i) 40 %, and (e, j) 50 %.

of the coating increases due to the presence of more defects, including particles and pores (Fig. 2). This leads to an uneven distribution of compaction force, poor contact between the coating and the carbon paper, and the formation of defects that obstruct the electron transmission path. Therefore, despite the increased Ta-N bond content and reduced Ta-O bond content in the TaN layer, the ICR value increases at higher N_2 ratios. At an N_2 ratio of 30 %, the coating surface is dense with a higher TaN content, resulting in the lowest ICR value of 6.85 mΩ·cm^2. Even after a 2 h polarization test at a constant potential of 0.6 V (SCE), the ICR value of the coating remains below 10 mΩ·cm^2. This indicates that the coating exhibits high stability in the PEMFC environment.

3.6. Coating adhesion test

To investigate the adhesion properties of TiN/TaN coatings under different N_2 ratios, adhesion tests were performed on all fresh samples using the grid method, as shown in Fig. 14. The results indicate that all coatings remained intact with no noticeable spalling. Based on the ASTM D3359 standard, all coatings achieved an adhesion grade of 5B, demonstrating excellent adhesion performance across all N_2 ratios. The strong adhesion between the TiN/TaN coating and the TC4 substrate can be attributed to several critical factors. Firstly, the Ti bonding layer between the TiN/TaN coating and the TC4 substrate establishes a robust metallic bond with both the substrate and the TiN transition layer. Additionally, it mitigates the mismatch in thermal expansion coefficients between the substrate and the TiN transition layer, thereby reducing interfacial stress and the risk of spalling, which collectively enhance the coating's overall adhesion. Secondly, cross-sectional morphology analysis reveals that the coating maintains a relatively thin profile across all N_2 ratios (< 1μm). A thinner coating generally exhibits lower internal stress, which enhances the bonding strength between the coating and the substrate. Moreover, across all N_2 ratios, the interfaces between the coating layers and between the coating and substrate are distinct and continuous, free of visible cracks, voids, or delamination. This structural integrity ensures the long-term stability of the coating during operation.

4. Conclusions

In this study, novel TiN/TaN coatings were prepared using RF magnetron sputtering and DC magnetron sputtering techniques at varying N_2 ratios for the surface modification of TC4 bipolar plates. The effects of different N_2 ratios on the surface structure, corrosion resistance, conductivity, and hydrophobicity of the coatings were investigated, and the main conclusions were as follows:

(1) With the increase of the N_2 ratio, the thickness of the TaN layer by DC sputtering decreases. In contrast, the thickness of the dense TiN layer by RF sputtering increases, and the proportion of nitride in the TaN layer improves. Furthermore, the TiN/TaN double-layer structure exhibits the highest compactness at a moderate N_2 ratio (30 %).

(2) Electrochemical tests indicated that the TiN/TaN coatings significantly improved the corrosion resistance of TC4 substrates. In particular, the TiN/TaN-30 % sample has the smallest defect density (2.657×10^{20} cm^{-3}) and the largest coating protection efficiency (97.8 %). Hence, its corrosion current density is as low as 0.152 μA/cm^2 and 0.628 μA/cm^2 in constant potential polarization tests at 0.6 V (SCE) and 1.1 V (SCE), respectively, this far below the 2025 DOE standard.

(3) The ICR tests and water contact angle tests show that the TiN/TaN-30 % sample obtained the lowest ICR value of only 6.85 mΩ·cm^2 under a compressive force of 140 N/cm^2, and the water contact angle as high as 95.5 °, which demonstrate that coating with excellent conductivity and hydrophobicity.

CRediT authorship contribution statement

Lintao Liu: Software, Investigation. **Xuan Li:** Software, Data curation. **Xiao Jiang:** Software, Data curation. **Can Xiong:** Software, Data curation. **Xiulan Li:** Formal analysis, Data curation. **Xinjun Zhou:** Formal analysis, Data curation, Conceptualization. **Yong Wang:** Writing – review & editing, Writing – original draft, Software, Investigation, Formal analysis, Data curation. **Yao Chen:** Software, Data curation. **Fei You:** Software, Data curation. **Wei Li:** Writing – review & editing, Investigation, Funding acquisition.

Declaration of Competing Interest

The authors declare that they have no known competing financial interests or personal relationships that could have appeared to influence the work reported in this paper.

Acknowledgment

This research was financially supported by the Key Research and Development Project of the Sichuan Province Science and Technology Department (No. 2023YFG0239), the Scientific Research and: Innovation Team Program of: Sichuan University of Science and Engineering (No. H92322), and the Graduate Innovation Fund Project of Sichuan University of Science & Engineering (No. Y2023080).

Declaration of competing interest

The authors declare no conflict of interest. The funders had no role in the design of the study, as well as in the collection, analyses, and interpretation of data, and will not have any role in the decision to publish the results.

Data Availability

Data will be made available on request.

References

[1] H. Ren, X. Meng, Y. Lin, Z. Shao, Independent regulation of ionomer distribution in catalyst layer for proton exchange membrane fuel cell, Electrochim. Acta 462 (2023) 142710, https://doi.org/10.1016/j.electacta.2023.142710.

[2] J.A. Turner, Sustainable hydrogen production, Science 305 (2004) 972–974, https://doi.org/10.1126/science.1103197.

[3] U. Babic, M. Suermann, F.N. Büchi, L. Gubler, T.J. Schmidt, Critical Review-identifying critical gaps for polymer electrolyte water electrolysis development, J. Electrochem. Soc. 164 (2017) F387–F399, https://doi.org/10.1149/2.1441704jes.

[4] M. Carmo, D.L. Fritz, J. Mergel, D. Stolten, A comprehensive review on PEM water electrolysis, Int. J. Hydrog. Energy 38 (2013) 4901–4934, https://doi.org/10.1016/j.ijhydene.2013.01.151.

[5] J. Jin, J. Zhang, M. Hu, X. Li, Investigation of high potential corrosion protection with titanium carbonitride coating on 316 l stainless steel bipolar plates, Corros. Sci. 191 (2021) 109757, https://doi.org/10.1016/j.corsci.2021.109757.

[6] T. Wilberforce, O. Ijaodola, E. Ogungbemi, F.N. Khatib, T. Leslie, Z. El-Hassan, J. Thomposon, A.G. Olabi, Technical evaluation of proton exchange membrane (pem) fuel cell performance-a review of the effects of bipolar plates coating, Renew. Sust. Energ. Rev. 113 (2019) 109286, https://doi.org/10.1016/j.rser.2019.109286.

[7] O. Ijaodola, E. Ogungbemi, F.N. Khatib, T. Wilberforce, M. Ramadan, Z.E. Hassan, J. Thompson, A.G. Olabi, Evaluating the effect of metal bipolar plate coating on the performance of proton exchange membrane fuel cells, Energies 11 (2018) 3203, https://doi.org/10.3390/en11113203.

[8] Z. Xu, D. Qiu, P. Yi, L. Peng, X. Lai, Towards mass applications: a review on the challenges and developments in metallic bipolar plates for pemfc, Prog. Nat. Sci. Mater. Int. 30 (2020) 815–824, https://doi.org/10.1016/j.pnsc.2020.10.015.

[9] H. Choi, H. Eun Kang, D.J. Kim, Y. Soo Yoon, A comprehensive review of stainless-steel bipolar plate coatings and their role in mitigating corrosion in aggressive proton-exchange membrane fuel cells environments, Chem. Eng. J. 493 (2024) 152662, https://doi.org/10.1016/j.cej.2024.152662.

[10] Y. Wang, S. Zhang, Z. Lu, L. Wang, W. Li, Preparation and performances of electrically conductive Nb-doped TiO_2 coatings for 316 stainless steel bipolar plates of proton-exchange membrane fuel cells, Corros. Sci. 142 (2018) 249–257, https://doi.org/10.1016/j.corsci.2018.07.034.

[11] M.F. Pillis, M.C.L. De Oliveira, R.A. Antunes, Surface chemistry and the corrosion behavior of magnetron sputtered niobium oxide films in sulfuric acid solution, Appl. Surf. Sci. 462 (2018) 344–352, https://doi.org/10.1016/j.apsusc.2018.08.123.

[12] K. Nikolov, K. Bunk, A. Jung, J.W. Gerlach, P. Kaestner, C.-P. Klages, Combined plasma surface modification of austenitic stainless steel for bipolar plates, Surf. Coat. Technol. 328 (2017) 142–151, https://doi.org/10.1016/j.surfcoat.2017.08.047.

[13] Y. Yu, S. Shironita, T. Mizukami, K. Nakatsuyama, K. Souma, M. Umeda, Corrosion-resistant characteristics of nitrided Ni-free stainless steel for bipolar plate of polymer electrolyte fuel cell, Int. J. Hydrog. Energy 42 (2017) 6303–6309, https://doi.org/10.1016/j.ijhydene.2017.01.211.

[14] Y. Yang, X. Ning, H. Tang, L. Guo, H. Liu, Effects of passive films on corrosion resistance of uncoated SS316L bipolar plates for proton exchange membrane fuel cell application, Appl. Surf. Sci. 320 (2014) 274–280, https://doi.org/10.1016/j.apsusc.2014.09.049.

[15] S. Peng, J. Xu, Z.H. Xie, Titanium bipolar plates augmented by nanocrystalline TiZrHfMoW coatings for application in proton exchange membrane fuel cells, Appl. Surf. Sci. 591 (2022) 153200, https://doi.org/10.1016/j.apsusc.2022.153200.

[16] T. Wilberforce, Z.E. Hassan, E. Ogungbemi, O. Ijaodola, F.N. Khatib, A comprehensive study of the effect of bipolar plate (BP) geometry design on the performance of proton exchange membrane (PEM) fuel cells, Renew. Sustain. Energy Rev. 111 (2019) 236–260, https://doi.org/10.1016/j.rser.2019.04.081.

[17] Q. Feng, X. Yuan, G. Liu, B. Wei, Z. Zhang, H. Li, H. Wang, A review of proton exchange membrane water electrolysis on degradation mechanisms and mitigation strategies, J. Power Sources 366 (2017) 33–55, https://doi.org/10.1016/j.jpowsour.2017.09.006.

[18] T.J. Toops, M.P. Brady, F.Y. Zhang, H.M. Meyer, K. Ayers, A. Roemer, L. Dalton, Evaluation of nitrided titanium separator plates for proton exchange membrane electrolyzer cells, J. Power Sources 272 (2014) 954–960, https://doi.org/10.1016/j.jpowsour.2014.09.016.

[19] M.F. Khan, A.Y. Adesina, Z.M. Gasem, Electrochemical and electrical resistance behavior of cathodic arc PVD TiN, CrN, AlCrN, and AlTiN coatings in simulated proton exchange membrane fuel cell environment, Mater. Corros. 70 (2019) 281–292, https://doi.org/10.1002/maco.201810377.

[20] K. Nikolov, K. Bunk, A. Jung, J.W. Gerlach, P. Kaestner, C.P. Klages, Combined plasma surface modification of austenitic stainless steel for bipolar plates, Surf. Coat. Technol. 328 (2017) 142–151, https://doi.org/10.1016/j.surfcoat.2017.08.047.

[21] U.K. Chanda, S.P. Padhee, A.K. Pandey, S. Roy, S. Pati, Nanostructured multilayer Cr/CrN coatings on 316 L stainless steel for proton exchange membrane fuel cell bipolar plates, Int. J. Hydrog. Energy 1904 (45) (2020) 21892, https://doi.org/10.1016/j.fuel.2024.132761.

[22] P.P. Gao, Z.Y. Xie, O.Y. Chun, T. Tao, X.B. Wu, Q.Z. Huang, Electrochemical characteristics and interfacial contact resistance of Ni-P/TiN/PTFE coatings on Ti bipolar plates, J. Solid State Electrochem 22 (2018) 1971, https://doi.org/10.1007/s10008-018-3896-0.

[23] N.B. Huang, H. Yu, L.S. Xu, S. Zhan, M. Sun, D.W. Kirk, Corrosion kinetics of 316L stainless steel bipolar plate with chromiumcarbide coating in simulated PEMFC cathodic environment, Results Phys. 6 (2016) 730–736, https://doi.org/10.1016/j.rinp.2016.10.002.

[24] Y.Q. Hu, F. Chen, Z.D. Xiang, Cr2N coated martensitic stainless steels by pack cementation process as materials for bipolar plates of proton exchange membrane fuel cells, J. Power Sources 414 (2019) 167–173, https://doi.org/10.1016/j.jpowsour.2019.01.002.

[25] Y. Vengesa, A. Fattah-alhosseini, H. Elmkhah, O. Imantalab, Investigation of corrosion and tribological characteristics of annealed CrN/CrAlN coatings deposited by CAE-PVD, Surf. Coat. Technol. 432 (2022) 128090, https://doi.org/10.1016/j.ceramint.2022.09.286.

[26] Y. Show, Electrically conductive amorphous carbon coating on metal bipolar plates for PEFC, Surf. Coat. Technol. 202 (2007) 1252, https://doi.org/10.1016/j.surfcoat.2007.07.065.

[27] O. Lavigne, C. Alemany-Dumont, B. Normand, P. Delich`ere, A. Descamps, Cerium insertion in 316 L passive film: Effect on conductivity and corrosion resistance performances of metallic bipolar plates for PEM fuel cell application, Surf. Coat. Technol. 205 (2010) 1870–1877, https://doi.org/10.1016/J.SURFCOAT.2010.08.051.

[28] M. Dadfar, M. Salehi, M.A. Golozar, S. Trasatti, M.P. Casaletto, Surface and corrosion properties of modified passive layer on 304 stainless steel as bipolar plates for PEMFCs, Int. J. Hydrog. Energen 42 (2017) 25869–25876, https://doi.org/10.1016/j.ijhydene.2017.08.169.

[29] H.Q. Fan, D.D. Shi, X.Z. Wang, J.L. Luo, J.Y. Zhang, Q. Li, Enhancing through-plane electrical conductivity by introducing Au microdots onto TiN coated metal bipolar plates of PEMFCs, Int. J. Hydrog. Energen 45 (2020) 29442–29448, https://doi.org/10.1016/j.ijhydene.2020.07.270.

[30] V. Bonu, M. Jeevitha, V. Praveen Kumar, S. Bysakh, H.C. Barshilia, Ultra-thin multilayered erosion resistant Ti/TiN coatings with stress absorbing layers, Appl. Surf. Sci. 478 (2019) 872–881, https://doi.org/10.1016/j.apsusc.2019.02.012.

[31] J. Jin, H. Liu, D. Zheng, Z. Zhu, Effects of Mo content on the interfacial contact resistance and corrosion properties of CrN coatings on SS316L as bipolar plates in simulated PEMFCs environment, Int. J. Hydrog. Energy 43 (2018) 10048–10060, https://doi.org/10.1016/j.ijhydene.2018.04.044.

[32] D. Zhang, L. Duan, L. Guo, Z. Wang, J. Zhao, W.H. Tuan, K. Niihara, TiN-coated titanium as the bipolar plate for PEMFC by multi-arc ion plating, Int. J. Hydrog. Energy 36 (2011) 9155–9161, https://doi.org/10.1016/j.ijhydene.2011.04.123.

[33] P. Yi, C. Dong, T. Zhang, K. Xiao, Y. Ji, J. Wu, X. Li, Effect of plasma electrolytic nitriding on the corrosion behavior and interfacial contact resistance of titanium in the cathode environment of proton-exchange membrane fuel cells, J. Power Sources 418 (2019) 42–49, https://doi.org/10.1016/j.jpowsour.2019.02.043.

[34] T. Li, Z. Yan, Z. Liu, Y. Yan, Y. Chen, Surface microstructure and performance of TiN monolayer film on titanium bipolar plate for PEMFC, Int. J. Hydrog. Energy 46 (2021) 31382–31390, https://doi.org/10.1016/j.ijhydene.2021.07.021.

[35] H.S. Heo, S.J. Kim, Investigation of Electrochemical characteristics and interfacial contact resistance of TiN-coated titanium as bipolar plate in polymer electrolyte membrane fuel cell, Coatings 13 (2023) 123, https://doi.org/10.3390/coatings13010123.

[36] C. Choe, H. Choi, W. Hong, J.J. Lee, Tantalum nitride coated AISI 316 L as bipolar plate for polymer electrolyte membrane fuel cell, Int. J. Hydrog. Energy 37 (2012) 405–411, https://doi.org/10.1016/j.ijhydene.2011.09.060.

[37] T.J. Pan, Y.J. Dai, J. Jiang, J.H. Xiang, Q.Q. Yang, Y.S. Li, Anti-corrosion performance of the conductive bilayer CrC/CrN coated 304SS bipolar plate in acidic environment, Corros. Sci. 206 (2022) 110495, https://doi.org/10.1016/j.corsci.2022.110495.

[38] S. Jannat, H. Rashtchi, M. Atapour, M.A. Golozar, H. Elmkhah, M. Zhiani, Preparation and performance of nanometric Ti/TiN multi-layer physical vapor deposited coating on 316 L stainless steel as bipolar plate for proton exchange membrane fuel cells, J. Power Sources 435 (2019) 226818, https://doi.org/10.1016/j.jpowsour.2019.226818.

[39] S. Wang, M. Hou, Q. Zhao, Y. Jiang, Z. Wang, H. Li, Y. Fu, Z. Shao, Ti/(Ti,Cr)N/CrN multilayer coated 316 L stainless steel by arc ion plating as bipolar plates for proton exchange membrane fuel cells, J. Energy Chem. 26 (2017) 168–174, https://doi.org/10.1016/j.jechem.2016.09.004.

[40] A. Shanaghi, S. Ghasemi, P.K. Chu, S. Ahangarani, Y. Zhao, Effect of Ti interlayer on corrosion behavior of nanostructured Ti/TiN multilayer coating deposited on TiAl6V4, Mater. Corros. 70 (2019) 2113–2127, https://doi.org/10.1002/maco.201910883.

[41] R. Li, Y. Cai, K. Wippermann, W. Lehnert, The Electrochemical Behavior of CrN/Cr Coatings with Defects on 316L Stainless Steel in the Simulated Cathodic

Environment of an HT-PEFC, J. Electrochem. Soc. 166 (2019) C394–C400, https://doi.org/10.1149/2.0591913jes.
[42] M. Alishahi, F. Mahboubi, S.M. Mousavi Khoie, M. Aparicio, E. Lopez-Elvira, J. Méndez, R. Gago, Structural properties and corrosion resistance of tantalum nitride coatings produced by reactive DC magnetron sputtering, RSC Adv. 6 (2016) 89061–89072, https://doi.org/10.1039/C6RA17869C.
[43] J.Y. Chen, S. Zhang, J. Zheng, Y.F. Dong, C.X. Zhang, J.C. Li, Z.L. Chen, J. Zhang, D. Sun, Excellent anti-corrosion and conductivity of NbN coated on Ti bipolar plate by controlling N_2 flow rates, J. Alloy. Compd. 976 (2024) 173033, https://doi.org/10.1016/j.jallcom.2023.173033.
[44] G. Greczynski, L. Hultman, Reliable determination of chemical state in x-ray photoelectron spectroscopy based on sample-work-function referencing to adventitious carbon: resolving the myth of apparent constant binding energy of the C 1 s peak, 99-03, Appl. Surf. Sci. 451 (2018), https://doi.org/10.1016/j.apsusc.2018.04.226.
[45] D.K. Jiao, X.F. Luo, Y.P. Hou, Y.Y. Zhang, D. Hao, Research on the durability degradation evaluation method of metal bipolar plate for proton exchange membrane fuel cells, Chin. Battery Ind. (2024) 1–6. ⟨https://link.cnki.net/urlid/32.1448⟩.
[46] A. Kumar, M. Ricketts, S. Hirano, Exsitu evaluation of nanometer range gold coating on stainless steel substrate for automotive polymer electrolyte membrane fuel cell bipolar plate, J. Power Sources 195 (2010) 1401–1407, https://doi.org/10.1016/j.jpowsour.2009.09.022.
[47] H. Zhang, H. Li, M. Fang, Z. Wang, L. Sang, L. Yang, Q. Chen, Roll-to-roll DBD plasma pretreated polyethylene web for enhancement of Al coating adhesion and barrier property, Appl. Surf. Sci. 388 (2016) 539–545, https://doi.org/10.1016/j.apsusc.2015.10.146.
[48] J. Xu, X.K. Bao, T. Fu, Y. Lyu, P. Munroe, Z.-H. Xie, In vitro biocompatibility of a nanocrystalline β-Ta_2O_5 coating for orthopaedic implants, Ceram. Int. 44 (2018) 4660–4675, https://doi.org/10.1016/j.ceramint.2017.12.040.
[49] M. Zhang, Y. Wang, S. Song, R. Guo, W. Zhang, C. Li, J. Wei, P. Jiang, R. Yang, Influence of room-temperature oxidation on stability and performance of reactively sputtered TaN thin films for high-precision sheet resistors, Surf. Interfaces 46 (2024) 104088, https://doi.org/10.1016/j.surfin.2024.104088.
[50] C.C. Chang, J.S. Jeng, J.S. Chen, Microstructural and electrical characteristics of reactively sputtered Ta-N thin films, Thin Solid Films 413 (2002) 46–51, https://doi.org/10.1016/S0040-6090(02)00342-5.
[51] E. Niu, L. Li, G. Lv, W. Feng, H. Chen, S. Fan, S. Yang, X. Yang, Synthesis and characterization of tantalum nitride films prepared by cathodic vacuum arc technique, Appl. Surf. Sci. 253 (2007) 5223–5227, https://doi.org/10.1016/j.apsusc.2006.11.042.
[52] A.C. Hee, Y. Zhao, S.S. Jamali, A. Bendavid, P.J. Martin, H. Guo, Characterization of tantalum and tantalum nitride films on Ti6Al4V substrate prepared by filtered cathodic vacuum arc deposition for biomedical applications, Surf. Coat. Technol. 365 (2019) 24–32, https://doi.org/10.1016/j.surfcoat.2018.05.007.
[53] X. Yang, E. Aydin, H. Xu, J. Kang, M. Hedhili, W. Liu, Y. Wan, J. Peng, C. Samundsett, A. Cuevas, S. De Wolf, Tantalum nitride electron-selective contact for crystalline silicon solar cells, Adv. Energy Mater. 8 (2018) 1800608, https://doi.org/10.1002/aenm.201800608.
[54] P. Lamour, P. Fioux, A. Ponche, M. Nardin, M. Vallat, P. Dugay, J. Brun, N. Moreaud, J. Pinvidic, Direct measurement of the N_2 content by XPS in self-passivated TaN_x thin films, Surf. Interface Anal. 40 (2008) 1430–1437, https://doi.org/10.1002/sia.2919.
[55] S. Jannat, H. Rashtchi, M. Atapour, M.A. Golozar, H. Elmkhah, M. Zhiani, Preparation and performance of nanometric Ti/TiN multi-layer physical vapor deposited coating on 316 L stainless steel as bipolar plate for proton exchange membrane fuel cells, J. Power Sources 435 (2019) 226818, https://doi.org/10.1016/j.jpowsour.2019.226818.
[56] X.Z. Wang, M.M. Zhang, Q. Hu, S. Su, H.Q. Fan, H. Wang, J.L. Luo, Optimizing the interfacial potential distribution to mitigate high transient potential induced dissolution on C/Ti coated metal bipolar plates used in PEMFCs, Corros. Sci. 208 (2022) 110686, https://doi.org/10.1016/j.corsci.2022.110686.
[57] N.D. Nam, J.H. Ahn, N.E. Lee, J.G. Kim, Electrochemical evaluation of the reliability of plasma-polymerized methylcyclohexane films, Mater. Res. Bull. 45 (2010) 269–274, https://doi.org/10.1016/j.materresbull.2009.12.024.
[58] K. Feng, Y. Shen, D. Liu, P.K. Chu, X. Cai, Ni–Cr Co-implanted 316 L stainless steel as bipolar plate in polymer electrolyte membrane fuel cells, Int. J. Hydrog. Energy 35 (2010) 690–700, https://doi.org/10.1016/j.ijhydene.2009.10.106.
[59] O. Sharifahmadian, A. Pakseresht, K.K. Amirtharaj Mosas, D. Galusek, Doping effects on the tribological performance of diamond-like carbon coatings: A review, J. Mater. Res. Technol. 27 (2023) 7748–7765, https://doi.org/10.1016/j.jmrt.2023.11.132.
[60] L. Castanheira, M. Bedouet, A. Kucernak, G. Hinds, Influence of microporous layer on corrosion of metallic bipolar plates in fuel cells, J. Power Sources 418 (2019) 147–151, https://doi.org/10.1016/j.jpowsour.2019.02.005.
[61] S. Ren, C. Du, Z. Liu, X. Li, J. Xiong, S. Li, Effect of fluoride ions on corrosion behaviour of commercial pure titanium in artificial seawater environment, Appl. Surf. Sci. 506 (2020) 144759, https://doi.org/10.1016/j.apsusc.2019.144759.
[62] Y. Guo, H.P. Chen, R.Y. Li, J.T. Geng, Z.G. Shao, Nb-Cr-C coated titanium as bipolar plates for proton exchange membrane fuel cells, J. Power Sources 520 (2022) 230797, https://doi.org/10.1016/j.jpowsour.2021.230797.
[63] A. Ingle, V. Raja, J. Rangarajan, P. Mishra, Corrosion resistant quaternary Al-CrMo-N coating on type 316 L stainless steel bipolar plates for proton exchange membrane fuel cells, Int. J. Hydrog. Energy 45 (2020), https://doi.org/10.1016/j.ijhydene.2019.11.119, 3094-3017.
[64] J. Jin, Z. He, X. Zhao, Formation of a protective TiN layer by liquid phase plasma electrolytic nitridation on Ti-6Al-4V bipolar plates for PEMFC, Int. J. Hydrog. Energy 45 (2020) 12489–12500, https://doi.org/10.1016/j.ijhydene.2020.02.152.
[65] S.P. Mani, P. Agilan, M. Kalaiarasan, K. Ravichandran, N. Rajendran, Y. Meng, Effect of multilayer CrN/CrAlN coating on the corrosion and contact resistance behavior of 316 L SS bipolar plate for high temperature proton exchange membrane fuel cell, J. Mater. Sci. Technol. 97 (2022) 134–146, https://doi.org/10.1016/j.jmst.2021.04.043.
[66] M. Liu, X. Cheng, X. Li, Y. Pan, J. Li, Effect of Cr on the passive film formation mechanism of steel rebar in saturated calcium hydroxide solution, Appl. Surf. Sci. 389 (2016) 1182–1191, https://doi.org/10.1016/j.apsusc.2016.08.074.
[67] R. Jiang, C. Chen, S. Zheng, The non-linear fitting method to analyze the measured M-S plots of bipolar passive films, Electrochim. Acta 55 (2010) 2498–2504, https://doi.org/10.1016/j.electacta.2009.11.093.
[68] Y. Chen, J. Xu, Z.H. Xie, P. Munroe, Nanocrystalline TaCN coated titanium bipolar plate dedicated to proton exchange membrane fuel cell, Ceram. Int 48 (2022) 19217–19231, https://doi.org/10.1016/j.ceramint.2022.03.214.
[69] C. Liu, Q. Bi, A. Matthews, EIS comparison on corrosion performance of PVD TiN and CrN coated mild steel in 0.5 M NaCl aqueous solution, Corros. Sci. 43 (2001) 1953–1961, https://doi.org/10.1016/S0010-938X(00)00188-8.
[70] L. Mølmen, L. Fast, A. Lundblad, P. Eriksson, P. Leisner, Contact resistance measurement methods for PEM fuel cell bipolar plates and power terminals, J. Power Sources 555 (2023) 232341, https://doi.org/10.1016/j.jpowsour.2022.232341.
[71] A. Chen, J. Jiang, X. Li, J. Hou, Z. Ding, B. Gan, K. Zhang, Formation and effect of hierarchical structures on corrosion performance of stainless steel bipolar plate fabricated by powder bed fusion, Corros. Sci. 219 (2023) 111193, https://doi.org/10.1016/j.corsci.2023.111193.
[72] L. Mendizabal, A. Oedegaard, O.E. Kongstein, S. Lædre, J. Walmsley, J. Barriga, J. J. Gonzalez, TaN_X coatings deposited by HPPMS on SS316L bipolar plates for polymer electrolyte membrane fuel cells: Correlation between corrosion current, contact resistance and barrier oxide film formation, Int. J. Hydrog. Energy 42 (2017) 3259–3270, https://doi.org/10.1016/j.ijhydene.2017.01.070.
[73] J. Jin, X. Kou, X. Tian, Y. Tao, X. Xu, H. Yang, Y. Mi, Investigation of corrosion protection with conductive chromium-aluminum carbonitride coating on metallic bipolar plates, Vacuum 213 (2023) 112084, https://doi.org/10.1016/j.vacuum.2023.112084.
[74] S. Li, S. Li, D.G. Wu, S. Wang, B.Z. Yang, H.B. Yang, X.G. Li, X.W. Zhang, Effect and mechanism of bias voltage on microstructure and corrosion resistance of Cr_xN_y coatings in proton-exchange membrane fuel cells, Vacuum 226 (2024) 113337.